ORIGINAL ARTICLE

DEM modeling of soil bottom-initiated radial desiccation cracking phenomenon

Wei-Jie Liu[1] · Chao-Sheng Tang[1] · Zhu-Yuan Lin[2] · Qing Cheng[1] · Yang Lu[3] · Tao Zhao[4] · Zhan-Ming Yang[1] · Wen Mu[1] · Chun Liu[1] · Bin Shi[1]

Abstract

Bottom-initiated radial cracking is a special phenomenon for soil as it is subjected to desiccation. This study aims to simulate the initiation and propagation of radial cracks in soil using both experimental and discrete-element method (DEM) approaches. Under controlled conditions of constant temperature and humidity, a laboratory desiccation test of clayey soil samples with bottom-constrained boundary conditions was carried out to illustrate the soil bottom-initiated radial desiccation cracking behavior. The evaporation characteristics as well as the development of radial cracking initiating from the subsoil were captured. To simulate this phenomenon, a desiccation model based on discrete-element method was used in DEM. Based on the laboratory testing results, appropriate parameters are selected for the numerical simulations. The DEM approach was calibrated by reproducing the experimental results of radial desiccation cracking. Subsequently, the initiation and propagation mechanisms of this typical soil cracking phenomenon was analyzed and discussed. With the constraint of the bottom boundary, the initiation of radial desiccation cracking was associated with the arched distribution of inter-particle tensile force in the soil samples. The propagation direction of the cracks was perpendicular to the inter-particle tensile forces. Finally, the effects of basal friction, evaporation gradient and shrinkage parameter on the bottom-initiated radial cracks in the simulation were analyzed. The size of the bottom particles and interface bonding factor played a significant role in the effect of basal friction. Compared with the samples under uniform water loss conditions, the bottom shrinkage rate was relatively low for the sample under a gradient water loss. In addition, an increase in the shrinkage parameter of the soil particles led to a greater extent of crack propagation.

Keywords Soil desiccation cracking · Radial cracks · Discrete-element method (DEM) · Tensile force · Influencing factors · Basal friction

---

✉ Chao-Sheng Tang
tangchaosheng@nju.edu.cn

Wei-Jie Liu
mg21290064@smail.nju.edu.cn

Zhu-Yuan Lin
lin@neq.ess.sci.osaka-u.ac.jp

Qing Cheng
chengqing@nju.edu.cn

Yang Lu
luy@hhu.edu.cn

Tao Zhao
tao.zhao@brunel.ac.uk

Zhan-Ming Yang
yangzhanming@smail.nju.edu.cn

Wen Mu
mg21290065@smail.nju.edu.cn

Chun Liu
chunliu@nju.edu.cn

Bin Shi
shibin@nju.edu.cn

1 School of Earth Sciences and Engineering, Nanjing University, 163 Xianlin Avenue, Nanjing 210023, China

2 Department of Earth and Space Science, Osaka University, 1-1 Machikaneyamacho, Toyonaka, Osaka 560-0043, Japan

3 College of Water Conservancy and Hydropower Engineering, Hohai University, No.1 Xikang Road, Nanjing 210098, China

4 Department of Civil and Environmental Engineering, Brunel University London, London UB8 3PH, UK

Introduction

Extreme drought climate conditions could usually lead to severe soil desiccation cracking phenomenon. The presence of cracks can significantly alter the strength, permeability, and compressibility of soils, reducing the overall stability and bearing capacity of the relevant earthworks (Péron et al. 2009; Sima et al. 2014; Tang et al. 2021). Soil desiccation cracking is of great importance in the environmental geotechnical engineering (Morris et al. 1992; Miller et al. 1998; Lozada et al. 2015), as it could potentially cause instability and serious failure of enclosed isolation layers in some fields, including nuclear waste storage and landfill (Nahlawi and Kodikara 2006; Rayhani et al. 2007; Kalkan 2009; Chaduvula et al. 2017). Furthermore, road subgrade cracking in pavement engineering and landslide in natural slopes are also common hazards due to soil desiccation cracking (Baker 1981; DeCarlo and Shokri 2014; Jiang et al. 2019; Xu et al. 2022).

Previous research on desiccation cracking mainly focuses on soil surface-initiated cracks, while limited attention has been given to desiccation cracks initiated at the soil bottom. It is widely recognized that water loss from the soil surface leads to surface-initiated desiccation cracking. In nature, soil sediments are typically stratified, while some desiccation cracks could also initiate within the subsoil and propagate toward the earth surface. For instance, Weinberger (1999) first reported that cracks can initiate from the subsoil, which has greatly changed the original understanding. Costa et al. (2013) also observed bottom-initiated cracks while conducting a series of desiccation cracking tests on potato starch samples. Despite subsurface cracks being easily overlooked due to difficulties in visualization, their initiation and propagation can lead to severe failure of soil structures. Consequently, the soil hydraulic–mechanical behaviors such as water retention capacity, permeability and strength can be significantly affected. The adverse effects and potential disasters caused by desiccation cracks in drought-prone regions might be underestimated if the cracks on unexposed surfaces are ignored, leading to more substantial losses (Lakshmikantha et al. 2013). Therefore, a comprehensive study on bottom-initiated cracks is of great significance in understanding the mechanism of this phenomenon and preventing the related disasters.

Recently, Zeng et al. (2020) changed the basal friction conditions of the slurry soil bars and conducted a series of desiccation tests. The experimental observations revealed a correlation between the propagation directions of cracks initiated at the bottom of the soil bar and their initiation positions. Vertical cracks tend to locate in the middle of the soil bar, while oblique cracks initiate near the edge which is called as radial cracks. They suggested that cracks initiated at the bottom surface and propagated obliquely upward are primarily influenced by the combined effect of shear and tensile stresses. Until now, comprehensive investigations into the mechanism of bottom-initiated radial cracks are still lacking due to the limitations of investigation methods.

In recent years, numerical modeling has become an effective approach in analyzing complex geotechnical engineering problems. Numerical methods could potentially overcome the shortcomings of experiments (e.g., time consuming and scale limitations), and enable multi-scale and multi-physics characterization of desiccation cracking in soils under a precisely controlled environment (Tang et al. 2021). Compared with other numerical methods, the discrete-element method (DEM) has an excellent adaptability to simulate discontinuous deformations and failure processes of granular materials (Cundall and Strack 1979). However, previous DEM simulations mainly focus on analyzing the two-dimensional crack network pattern and geometry, while the initiation and propagation of a single crack in a 3D space of the sample are not well studied (Sima et al. 2014; Guo et al. 2018; Le et al. 2022). Vo et al. (2017) used a cohesive fracture method and proposed a hydro-mechanical coupling model to simulate the desiccation of clayey soil, in which the soil bottom-initiated cracking phenomenon was observed. Recently, Lin et al. (2021) have successfully modeled both top-initiated and bottom-initiated cracks in a thin clay layer using DEM. However, in their work, the propagation direction and angle of the cracks initiated from bottom were not presented. Up to now, quite a few numerical analyses on the bottom-initiated cracks exist, and the involved mechanism is still unclear. No attempt has been made to simulate the bottom-initiated radial desiccation cracking phenomenon in soil.

The main objective of this research is to investigate the initiation and propagation of radial cracks initiating from the soil–base interface using the discrete-element method. A laboratory soil desiccation test was first carried out on a clay sample with a bottom-constrained boundary condition. The development of the bottom-initiated radial cracks and the evaporation characteristics during the drying process were monitored. Based on the laboratory testing results, a two-dimensional desiccation model based on DEM was employed to capture the initiation and propagation mechanisms of the bottom-initiated soil radial desiccation cracking phenomenon, considering the variability of soil properties. The DEM approach was also validated by reproducing the results of experimental radial desiccation cracking. The involved mechanisms and the parameter sensitivity of the model were analyzed.

Laboratory tests

Materials and methods

The soil used in laboratory tests was sampled from Nanjing, China. The physical properties of the soil are presented in Table 1. It is classified as a lean clay (CL) according to the Unified Soil Classification System (ASTM D-2487, 2017). To obtain a relatively homogeneous sample, the natural clayey soils were subjected to air drying, crushing, and passing through a 2 mm sieve. Oversaturated slurry samples were prepared by mixing the sieved clay with distilled water to reach an initial gravimetric water content of 170%. The sample was vibrated on a shaking table for about 5 min to remove entrapped air bubbles generated in clay slurry. Subsequently, it was sealed and stored for 72 h to achieve a water content equilibrium state. After sedimentation, the water above the slurry surface was pumped and the gravimetric water content of the sample was further measured as 58.9%.

The acrylic container with the dimension of 90 mm (length) × 25 mm (width) × 40 mm (height) was used in the laboratory tests. The boundary confinement was achieved by fixing a sandpaper (the average sand grain diameter: 0.063 mm) to the bottom of the container. The container sidewalls were coated with grease to reduce the boundary effect. Subsequently, the prepared slurry was poured into the acrylic container to form a predetermined layer thickness of 35 mm. Ultimately, the desiccation tests were conducted under controlled room temperature of 25 °C, and relative humidity of 40%. The schematic drawing of the experimental setup is shown in Fig. 1. During the drying process, the sample weight and water evaporation rate were monitored, and the side views of the drying sample were recorded by a fixed digital camera at every 2 h.

Experimental results

The variations in water content (w) and evaporation rate (R_e, mass of water loss per minute) over time are illustrated in Fig. 2. The process of water evaporation can be described as three main stages during drying (Cui et al. 2010; Tang et al. 2011). At stage 1 (constant rate stage), the average evaporation rate was ~ 0.011 g/min, while the average water content decreased linearly from 58.9% to 16.4%. Stage 2 (rate decreasing stage) started at the average water content of 16.4% (corresponding to the air-entry value). After about

Table 1 Physical properties of the tested clayey soil

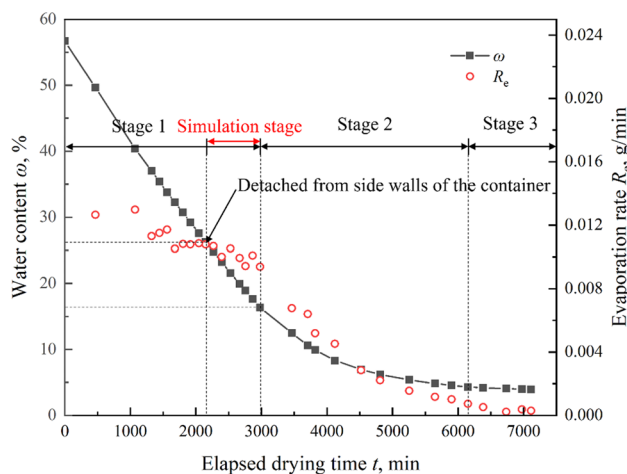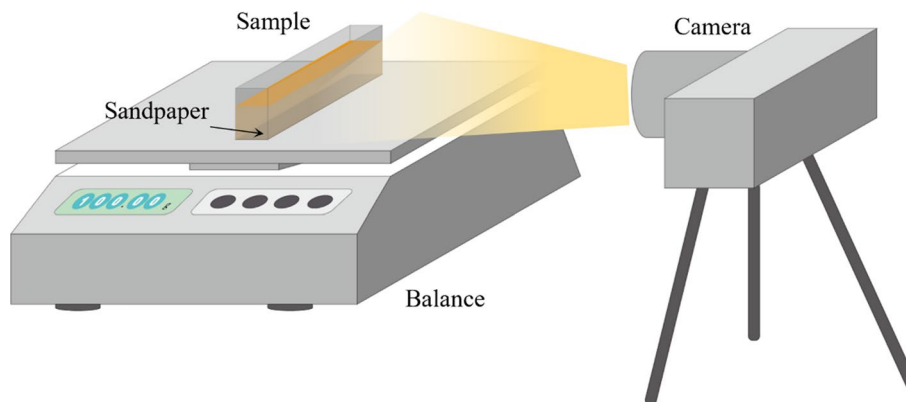| Soil properties	Value
Specific gravity	2.73
Liquid limit (%)	36.5
Plastic limit (%)	19.5
Plasticity index (%)	17.0
Sand content (%)	2
Silt content (%)	76
Clay content (%)	22
USCS classification	CL

Fig. 2 Changes of the water content and evaporation rate during the desiccation tests

Fig. 1 Schematic drawing of the experimental setup

2980 min, the decrease of water content slowed down gradually, and the corresponding water evaporation rate decreased rapidly. During stage 3 (residual rate stage), the residual water content of the soil sample stabilized at around 4.1%. Concurrently, the water evaporation rate approached zero upon attaining the residual water content.

Figure 3 illustrates the crack initiation and propagation in the tested sample with the change of water content. The slurry sample shrunk and completely detached from the two side walls of the container at the average water content of 26.2% and soil thickness of 30 mm. A series of preliminary tests in the early stage show that the effect of detaching from the walls of the container on the initiation and propagation of cracks is significant. If the sample did not detach completely from the container walls, the cracking initiated at the sample top or side surfaces is likely to be observed. This phenomenon can be explained by the boundary constraint provided by the cohesion between the side wall and the sample, leading to stress concentration at the detached and non-detached regions. The observations can match well the results reported from other studies on bottom crack initiation (Zeng et al. 2020; Lin et al. 2021).

As shown in Fig. 3, Crack 1 and Crack 2 initiated from the soil–base interface simultaneously at the average water content of 21.6% and propagated in oblique directions at the right edge of the sample. The soil was fully saturated at the crack initiation stage and the corresponding evaporation falls into the constant rate stage (Stage 1, Fig. 2), as indicated by Tang et al. (2011). Two bottom-initiated cracks (Crack 3 and Crack 4) at the left side edge and middle of the bottom boundary, respectively, initiated and propagated when the average water content decreased from 21.6% to 16.4%. This phenomenon is radial desiccation cracking where vertical cracks initiate in the middle of the sample, while oblique cracks initiate near the edge of the sample. Furthermore, the left-initiated cracks inclined to the left, while the right-initiated cracks inclined to the right. As the soil sample started to desaturate at the average water content of 16.4%, the number of cracks did not increase and only the crack width increased slightly. It should be noted that only the bottom-initiated cracks can be observed in the sample. All cracks initiated from the bottom and stopped in halfway at the end of drying process. This is attributed to the lower water content distribution in the upper soil mass, resulting in the formation of a higher tensile strength (Lin et al. 2021). At the end of test, slight curling phenomenon of the soil sample can be observed (Morris et al. 1992; Nahlawi and Kodikara 2002; Zeng et al. 2020).

Discrete-element modeling of soil desiccation

In the DEM model, the soil aggregates are usually simulated as spherical particles (Sima et al. 2014; Guo et al. 2018; Lin et al. 2021; Tran et al. 2021; Le et al. 2022). The discrete particles do not directly represent solid grains or dry clay particles, but represent the mixture of soil and water phases. A linear contact bond model (Itasca Consulting Group Inc., 2015) was selected as the fundamental model to simulate the cohesion between clayey soil particles. This contact model has also been successfully employed by previous researchers in DEM simulations of clayey soil behaviors (Guo et al. 2018; Gu et al. 2022).

It is generally believed that the desiccation cracking of clayed soils occurs when the internal tensile stress exceeds the tensile strength of the soil (Kodikara and Choi 2006;

Fig. 3 Crack patterns of the sample when water content is (**a**) 26.2%; (**b**) 23.2%; (**c**) 21.6%; (**d**) 18.9%; (**e**) 16.4%; (**f**) 4.1% (side view, serial number C1–C4 marks the initiation location and sequence of cracks)
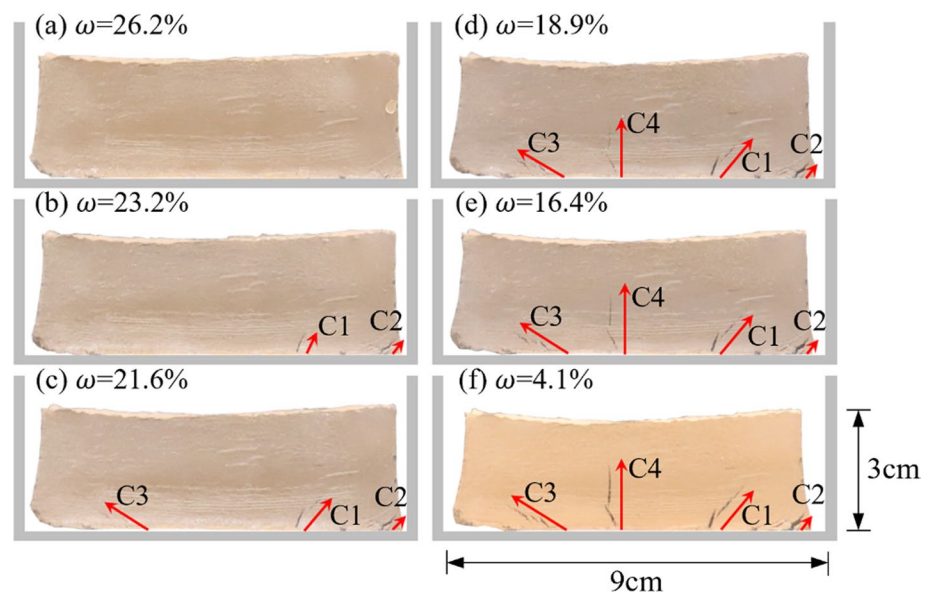
Tang et al. 2010). The concentration of tensile stress inside the soil is caused by the soil shrinkage constraint or non-uniform drying shrinkage during the drying process. In terms of the desiccation model, the shrinkage of the particles simulates the water loss of the saturated soils. When the shrinkage deformation is constrained, tensile force will also be generated between the particles. If the tensile force exceeds the tensile strength between the particles, the cohesive bond will break between the particles. The soil desiccation model is described in detail as below.

Contact model

The force–displacement relationship of the linear-elastic contact bond model is shown in Fig. 4. The normal and incremental tangential contact forces between bonded particles are calculated as

$$F_n = k_n d_n, \tag{1}$$

$$\Delta F_s = k_s \Delta d_s, \tag{2}$$

where k_n and k_s are the normal and tangential stiffness, and d_n and d_s are the normal and tangential displacement. The normal stiffness k_n can be obtained by the effective modulus E_c at the contact as follows (Potyondy and Cundall 2004):

$$k_n = \frac{A * E_c}{L}, \tag{3}$$

where A and L are the cross-section area and length at the contact in the two-dimensional model as follows:

$$A = 2rt(t = 1), r = \begin{cases} \min(R^{(1)}, R^{(2)}), \text{ball-ball} \\ R^{(1)}, \text{ball-wall} \end{cases}, \quad L = \begin{cases} R^{(1)} + R^{(2)}, \text{ball-ball} \\ R^{(1)}, \text{ball-wall} \end{cases}, \tag{4}$$

where $R^{(1)}$ and $R^{(2)}$ are the radii of the two contacting particles.

It is noted that how the contact force between particles is calculated in DEM based on the overlapping distance between the contacting particles at every step, while the particles are shrinking without moving during drying process. When the normal tensile force F_n between particles exceeds the tensile strength T_n or the tangential force F_s between particles exceeds the shear strength T_s, the cohesive bond breaks.

After the bond breakage, the model becomes a linear contact model for dispersed particles. The mechanical behavior is linear elastic and frictional with slip being accommodated by imposing a Coulomb limit on the shear force. The contact forces between dispersed particles are calculated by

$$F_n = \begin{cases} k_n d_n, d_n < 0 \\ 0, \text{otherwise} \end{cases}, \tag{5}$$

$$F_s^i = \begin{cases} F_s^{i-1} + k_s \Delta d_s, & F_s^{i-1} < \mu F_n \\ F_s^\mu = \mu F_n, & \text{otherwise} \end{cases}, \tag{6}$$

where F_s^i and F_s^{i-1} are shear forces calculated at the current and previous simulation time steps, respectively; Δd_s is the corresponding incremental shear displacement; μ is the friction coefficient.

Fig. 4 The force–displacement law of the bond contact model (k_n and k_s are normal and tangential stiffness, d_n and d_s are normal and tangential displacement, and F_s^μ is sliding friction force)
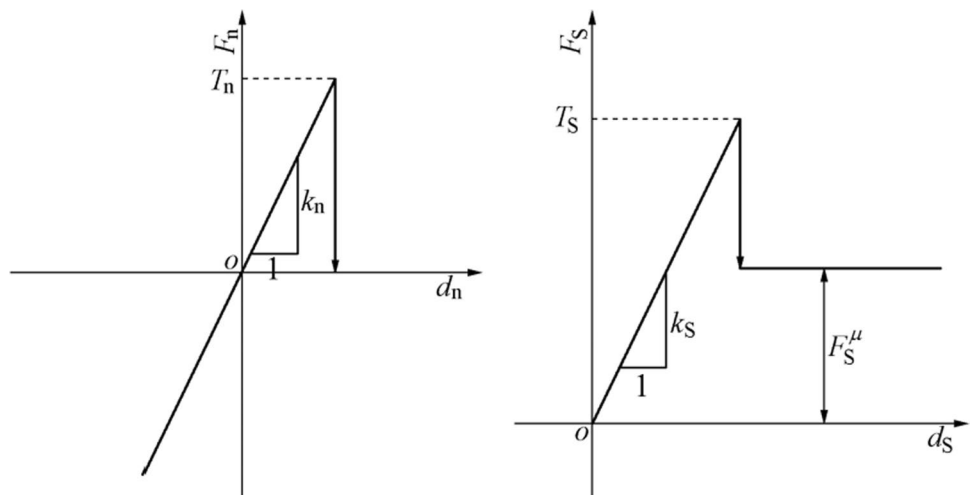
Changes of physical and mechanical properties during drying

Macroscopically, during the drying process, the clayey soil properties change simultaneously, including the physical (e.g., volume, density) and mechanical properties (e.g., contact forces). Therefore, the relationship between the corresponding meso-parameters and water content was established in the proposed model.

Volume

The majority of the desiccation cracks initiate during the first stage of evaporation, as shown in the Section "*Test results*", which is also consistent with the results obtained by previous researchers (Costa et al. 2008). During this stage, the soil is saturated, and the evaporation rate is a constant. While there might be localized unsaturation of the sample, the soil as a whole remains saturated (Shin and Santamarina 2011). The fundamental assumption of the model is that the soil is saturated, and the water loss due to evaporation leads to the change of volume and mass in the soil sample. The relationship between particle size and drying time needs to be established to reflect the dynamic changes of the volume in the DEM model. For samples with homogeneous shrinkage, El Youssoufi et al. (2005) proposed the relationship between the variation of particle radius R and drying time t:

$$R = R_0 e^{\left(-\alpha \frac{t}{T}\right)}, \tag{7}$$

where R_0 is the initial radius of the particles, α is the shrinkage parameter, and T is the total simulation time. Since the evaporation rate remains constant during the first stage of water evaporation, the variation over time in Eq. (7) can be substituted by the alteration in water content within the sample. Therefore, the equation of particle radius R variation can be rewritten as

$$R = R_0 e^{\left(-\alpha \frac{(w_0 - w)}{(w_0 - w_f)}\right)}, \tag{8}$$

where w_0, w and w_f are the initial water content, current water content and final water content in the simulation, respectively. Assuming the shrinkage kinetics is the same for all the discrete particles, the overall shrinkage deformation of the sample is consistent with the shrinkage deformation of a single particle. Therefore, in the two-dimensional model, the volumetric strain ε_v of the sample during the shrinkage process can be expressed as

$$\varepsilon_v = 1 - e^{\left(-2\alpha \frac{(w_0 - w)}{(w_0 - w_f)}\right)}. \tag{9}$$

The variable of α can be calculated by the following equation:

$$\alpha = -\frac{1}{2}\ln\left(1 - \varepsilon_{vf}\right), \tag{10}$$

where ε_{vf} is the final volumetric strain of the sample at the end of the simulation.

Density

During the process of soil drying, it is also necessary to consider the change in particle density. In DEM, the total mass of the solid phase is set to 1, and the mass of the liquid phase is equivalent to the current mass of water content. The following equation can be used to calculate the density of particles in the model under different water contents in the saturated state:

$$\rho_{sat} = \frac{1+w}{\frac{1}{G_s \rho_w} + \frac{w}{\rho_w}}, \tag{11}$$

where G_s is the specific gravity of the clayey soil in the laboratory test, and ρ_w is the density of water.

To ensure mass conservation during the simulation, the volumetric strain of the sample is determined by the change of water content in the saturating stage, which is a function of the initial and final water content:

$$\varepsilon_{vf} = 1 - \frac{V_f}{V_0} = 1 - \frac{\frac{1}{G_s \rho_w} + \frac{w_f}{\rho_w}}{\frac{1}{G_s \rho_w} + \frac{w_0}{\rho_w}}, \tag{12}$$

where V_0 is the initial particle volume and V_f is the final particle volume.

Mechanical properties

The tensile strength and elastic modulus of soil are major mechanical parameters controlling the development of tensile cracks (Tang et al. 2015), which can be calibrated by experimental data from direct tensile tests. The same method was also employed by Lin et al. (2021) and Sima et al. (2014). The DEM model of the test was set up as a composite of two wedges with 50.0 mm in width and 100.0 mm in length, as shown in Fig. 5a. The particle radius of the sample varied from 0.27 mm to 0.33 mm, with an average value of 0.30 mm. The particle size distribution is the same as that in the desiccation cracking simulation. The stress–strain curves were obtained by applying a constant displacement rate of 0.5 mm/min in opposite directions to the loading area at both ends of the sample, as shown in Fig. 5b. The peak value of the stress is taken as the macroscopic tensile strength of the samples, and the

Fig. 5 **a** The sample of tensile test in numerical simulation. **b** Stress–strain curves of the samples with different water contents
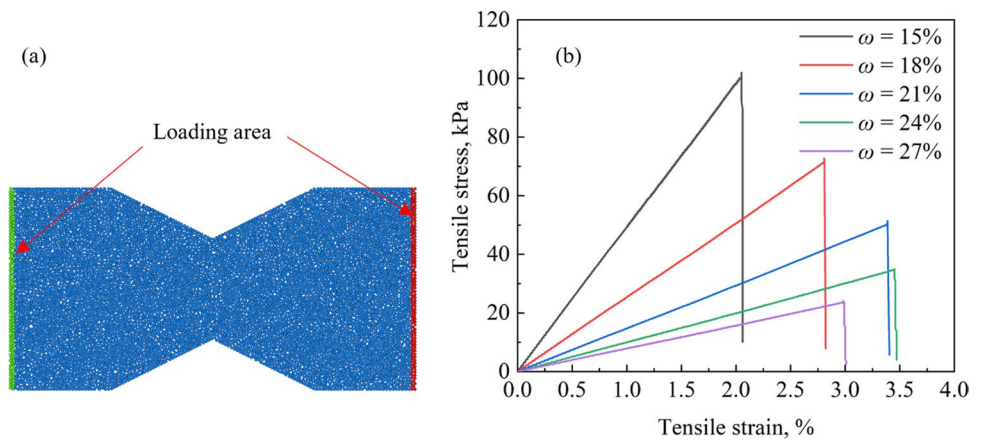
slope of the curve is the macroscopic elastic modulus. To simplify the calculation, the tensile strength is assumed to be equivalent to the shear strength, and the normal contact stiffness is consistent with the tangential contact stiffness in the contact model (Guo et al. 2018; Lin et al. 2021). The correlation between the tensile bond strength and effective modulus of the particles as a function of water content is established through parameter calibration in sections below.

Numerical model configurations

Initial model establishment and input parameters

The size of the sample container in the simulation was 30 mm in height and 90 mm in length. To obtain homogeneous samples, the grid method proposed by Duan et al. (2017) was used to generate the samples. The particle radius varied from 0.27 mm to 0.33 mm, with an average radius of 0.30 mm. The adopted particle size in this simulation may not be consistent with that of the laboratory tests due to high computational cost for real sized sample. However, our preliminary works have indicated that when the sample particle size is less than 0.4 mm, the size discrepancy does not impede the mechanical interpretation of the initiation and propagation mechanisms of radial desiccation cracking. The particle size in the simulation

governs the sample's structure and additionally influences the shape of the cracks formed during drying (Lin et al. 2021). As the particle size decreases, the edges of the developed cracks become smoother. Generally, it does not affect the overall reproduction of the drying process and cracking pattern. Nonetheless, a smaller particle size would result in a larger quantity of particles, leading to a significant reduction in the computational efficiency of the simulations. Therefore, the selection of particle size is based on the considerations of being able to track crack development clearly, while maintaining computational efficiency. A group of particles of radius 0.3 mm were fixed at the bottom of the sample to mimic the fixed boundary condition. The sample in the model was composed of 8246 particles. The bonds between the particles were added after the gravitational deposition. The geometry of the initial sample in the numerical model is shown in Fig. 6.

This research has investigated the constant rate stage of soil evaporation after the sample detached from two side walls of the container by PFC2D discrete-element software. The sample has the initial water content of 26.2% and the final water content of 16.4% corresponding to the water content of the air-entry value. In the simulation, the total volumetric strain ε_{vf} of water content from 26.2% to 16.4% was determined by Eq. (12) and the value of α was calculated by Eq. (10) as 0.085. Then, Eq. (8) is determined. As the water content changes, the particle radius (particle volume) does change. The time step in DEM simulation is

Fig. 6 The geometry of the initial sample in numerical simulation
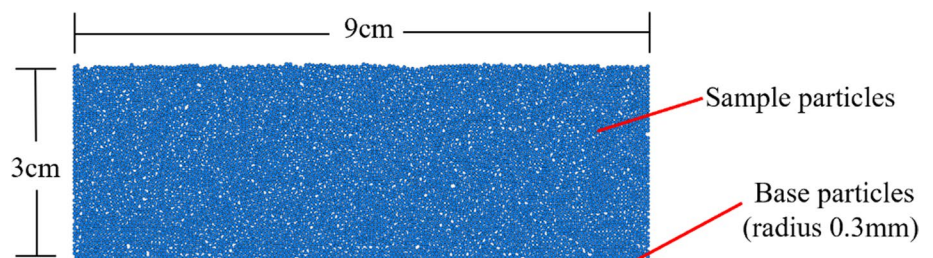
usually only a few microseconds, while the laboratory test usually lasts for several days. Therefore, it is unrealistic to control the amount of water evaporated in each iteration of DEM simulation according to the evolution of water content over time obtained from the laboratory test (Le et al. 2022). To improve the computational efficiency, it is set for every 0.01 s increase in simulation time, the water content of the sample decreases by 0.05%.

The changes of tensile strength σ_t (kPa) and elastic modulus E (MPa) of the soil with water content w (%) was obtained through laboratory tests according to Lin et al. (2021), as shown in the following equations:

$$\sigma_t = 680.143 e^{(-0.124w)}. \tag{13}$$

$$E = 0.736 + 229.3 e^{(-0.270w)}. \tag{14}$$

Accordingly, the tensile bond strength T_n (N) and effective modulus E_c (MPa) between particles were calibrated, and the relationship between these two parameters with the water content w (%) was obtained as follows:

$$T_n = 150.623 e^{(-0.124w)}. \tag{15}$$

$$E_c = 0.5 + 200.3 e^{(-0.270w)}. \tag{16}$$

Calibration results of the DEM model is shown in Fig. 7. The black line in Fig. 7 represents the tensile strength σ_t (kPa) and elastic modulus E (MPa) obtained from laboratory tests, varying with water content. The red line is the calibration results of macroscopic tensile strength (kPa) and elastic modulus (MPa) changing with

water content. They were obtained by inputting the tensile bond strength T_n (N) and effective modulus E_c (MPa) between discrete particles (derived from Eqs. (15) and (16)) into the model as a meso-parameter and conducting direct tensile tests. The calibration results show the tensile strength and elastic modulus in the DEM model match well the laboratory results. It should be noted that the simulation begins when the sample has detached from the walls of the container. Thus, no sidewall constraint was set on the sample. The bonds between the particles and the bottom boundary particles in the DEM simulation corresponds to the interaction between the soil sample and the bottom surface sandpaper in the laboratory test. The interface bonding factor d was added to account for the tensile strength between particles of the sample and the bottom boundary:

$$T_{n(soil-base)} = d * T_{n(soil-soil)}. \tag{17}$$

Table 2 Parameter in the numerical simulation

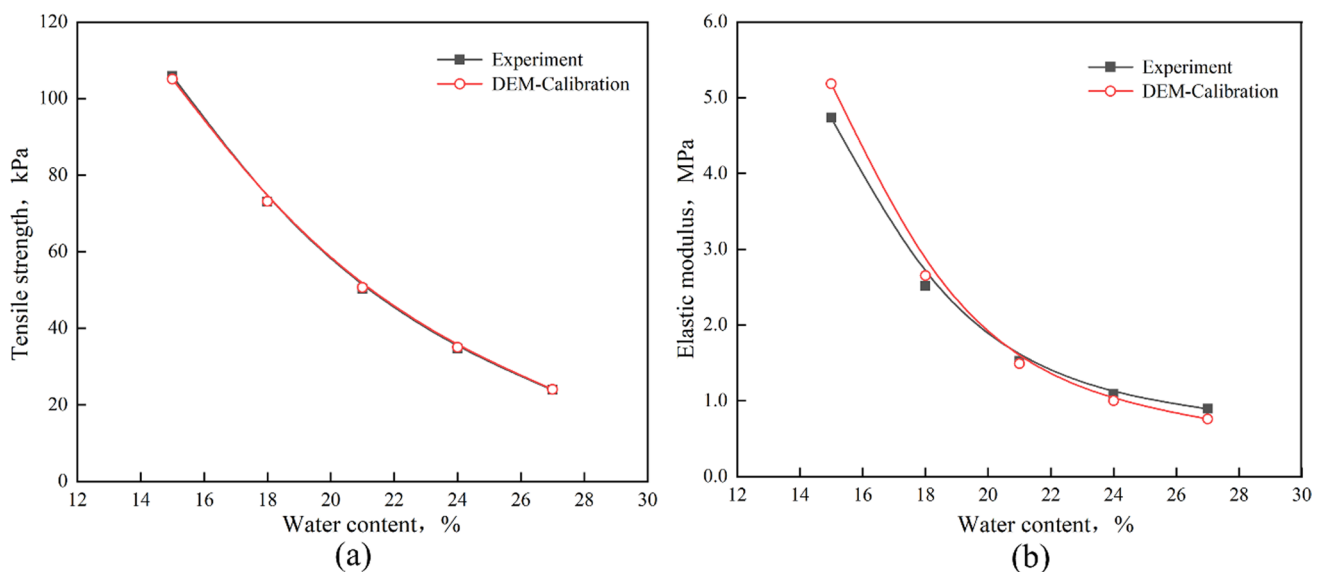| Parameter	Initial value	Final value
Particle density (kg/m^3)	2008	2195
Water content (%)	26.2	16.4
Average particle radius (mm)	0.300	0.276
Volume strain	0	0.156
Shrinkage parameter	0.085	
Effective modulus (MPa)	0.67	2.89
Bond strength (N)	5.84	19.71
Interface bond factor	1.0	
Friction coefficient	0.25	

Fig. 7 Calibration of the DEM model, (**a**) tensile strength and (**b**) elastic modulus

In the simulation, d was set as 1.0, and the friction coefficient between particles was 0.25. Table 2 summarizes the main input parameters used in the simulation of bottom-initiated radial cracking.

Results

Cracking pattern and force distribution of the sample during drying process

The soil sample cracking process is analyzed in terms of the force chain distribution and the cracking pattern, as shown in Fig. 8. The left plots (a–f) illustrate the evolution of soil cracking with the gradual decrease of water content. The middle plots (g–l) and the right plots (m–r) are diagrams of the distribution and magnitude of the force chain within the sample, respectively. In plots (g–l), the red lines represent the inter-particle tensile forces in the sample, while the black lines represent the inter-particle compressive forces. In addition, the green line segments represent the micro-cracks resulting from bond breakage between soil particles.

The initial cracking pattern and inter-particle force chain distribution of the sample at water content of 26.2% is shown in Fig. 8a, g, respectively. The densely spaced black lines observed at the bottom region indicate a relatively high compressive force in that area. The compressive force gradually decreases with the height. As the water content decreases, the basal friction constrained the shrinkage of the sample bottom region, resulting in the heterogeneous distribution of tensile forces there. The tensile forces were distributed in an arch shape. The thickest and most concentrated red lines were observed at the bottom of both sides of the sample, indicating the concentration of tensile force as shown in Fig. 8b, h. With the soil shrinkage developed further, the inter-particle tensile force at the bottom corners of the sample reached its tensile strength. Therefore, the inter-particle bonds at this position broke, resulting in micro-cracks. After cracking, the region of tensile stress in the arch-shaped distribution decreases and contracts towards the geometric center of the sample due to stress redistribution. The micro-cracks at the bottom further propagated into the main crack (Crack 1) on the bottom surface at the water
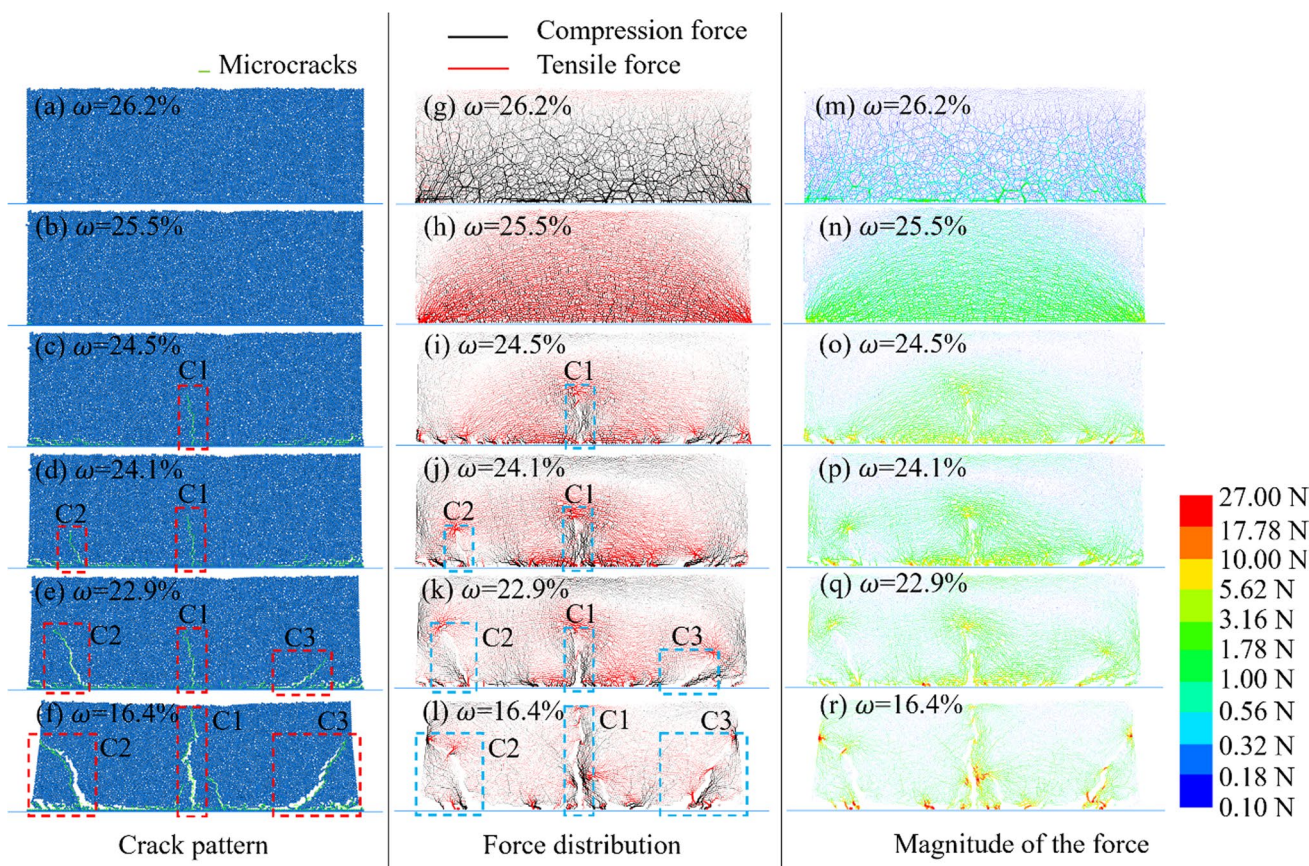

Fig. 8 Evolution of cracking pattern, the inter-particle force distribution and magnitude of the soil sample during drying process. **a–f** The crack pattern of the sample. **g–l** The inter-particle force chain distribution of the sample. **m–r** The magnitude of the inter-particle force inside the sample

content of 24.5%. The tensile forces concentrated at the top of the main cracks, and the cracks continued to propagate upwards. The main crack (Crack 2) appeared on the left side at a water content of 24.1%, but the crack pattern was not obvious on the macroscopic level. As the water content decreased, the main crack at the bottom propagated. It should be noted that the sequence of cracks development in the sample differs from the laboratory test. Cracks may first initiate from both the middle and edge regions of the sample, a phenomenon also observed in the laboratory test conducted by Zeng et al. (2020). In addition, it was observed that both sides of the sample curled upward due to the presence of tensile stress (Lin et al. 2022; Tran et al. 2020), which can also be observed in the laboratory test. The curling was primarily attributed to differential shrinkage of the sample induced by moisture gradient along the depth (Kodikara et al. 2004; Maedo et al. 2020; Lin et al. 2022). Specifically, the upper portion of the sample experienced a

higher degree of shrinkage, while the shrinkage of the bottom portion was constrained.

Figure 9 shows the view of the crack initiation process of Crack 1 (Fig. 9a–h) and Crack 2 (Fig. 9i–r). The middle cracks initiated vertically, while the cracks on both sides of the sample were inclined, which is similar to the experimental observations in Fig. 3. Figure 9a–h illustrates the cracking pattern and inter-particle force distribution during the initiation and propagation of Crack 1. As shown in Fig. 9e, the tensile force field exhibited an almost horizontal distribution prior to the initiation of Crack 1. With further shrinkage of the soil sample, vertical micro-cracks initiated sequentially upwards from the bottom boundary. The tensile force field concentrated at the tip of the Crack 1, and the crack continued to propagate upwards. Simultaneously, the force field on both sides of Crack 1 did not weaken entirely, leading to the ongoing development of micro-cracks at the bottom. Figures 9i–r shows the variations of the cracking pattern and inter-particle force distribution during the initiation and
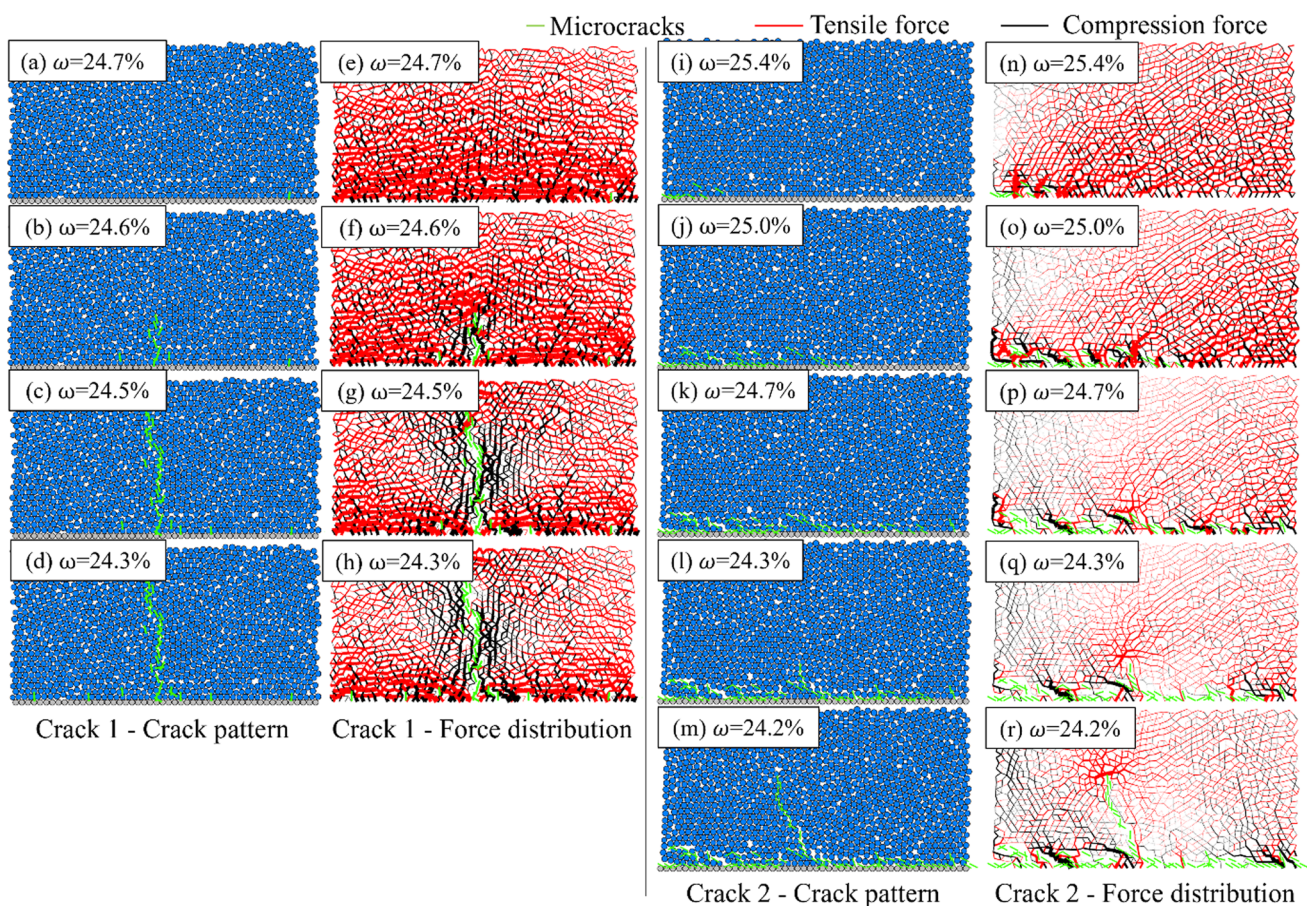

Fig. 9 Cracking pattern and the inter-particle force distribution during the initiation of Crack 1 and Crack 2. **a–d** The cracking pattern during the initiation process of Crack 1. **e–h** The inter-particle force distribution of the sample during the initiation of Crack 1. **i–m** The cracking pattern during the initiation process of Crack 2. **n–r** The inter-particle force distribution of the sample during the initiation process of Crack 2

development of Crack 2. As shown in Figs. 9n–p, the sample shrank centripetally, initiating a series of micro-cracks from left to right at the sample bottom boundary. The local tensile force field was inclined to the right, and the corresponding direction of the micro-cracks was mostly inclined to the left. As shown in Figs. 9l, q, the micro-cracks continued to develop at the water content of 24.3%. It is obvious that the tensile force was highly concentrated at the crack tip, driving the propagation of the crack to form Crack 2.

The adhesion and friction between the soil sample and side walls constrained the sample shrinkage, leading to the generation of the tensile forces in the sample, as shown in Fig. 10. When the side walls were added, it is apparent that the boundary conditions have a great effect on the inter-particle force distribution in the sample. As shown in

Fig. 10h, the force concentration occurred in the upper right side near the side wall. When the local inter-particle tensile force reached the tensile strength, the sample detached from the side walls. Without the constraint of the side walls, the inter-particle tensile force in the sample was redistributed as shown in Fig. 10j. Similar to the cases without sidewalls, the bottom boundary additionally constrained the shrinkage of the sample, resulting in the force concentration at the bottom edge of the sample. This phenomenon has also been observed in some previously published work on desiccation cracking simulations of soil bar (Péron et al. 2013; Sánchez et al. 2014; Lin et al. 2021). After cracking, the original soil bar is divided into several shorter soil bars, where the tensile force distribution is similar to the arched tensile force field, as depicted in Figs. 8h and 10j (Sánchez et al. 2014; Lin

Fig. 10 Evolution of cracking pattern and the inter-particle force distribution of the sample with side walls during drying in numerical simulations. **a–f** The crack pattern of the sample. **g–l** The inter-particle force distribution of the sample
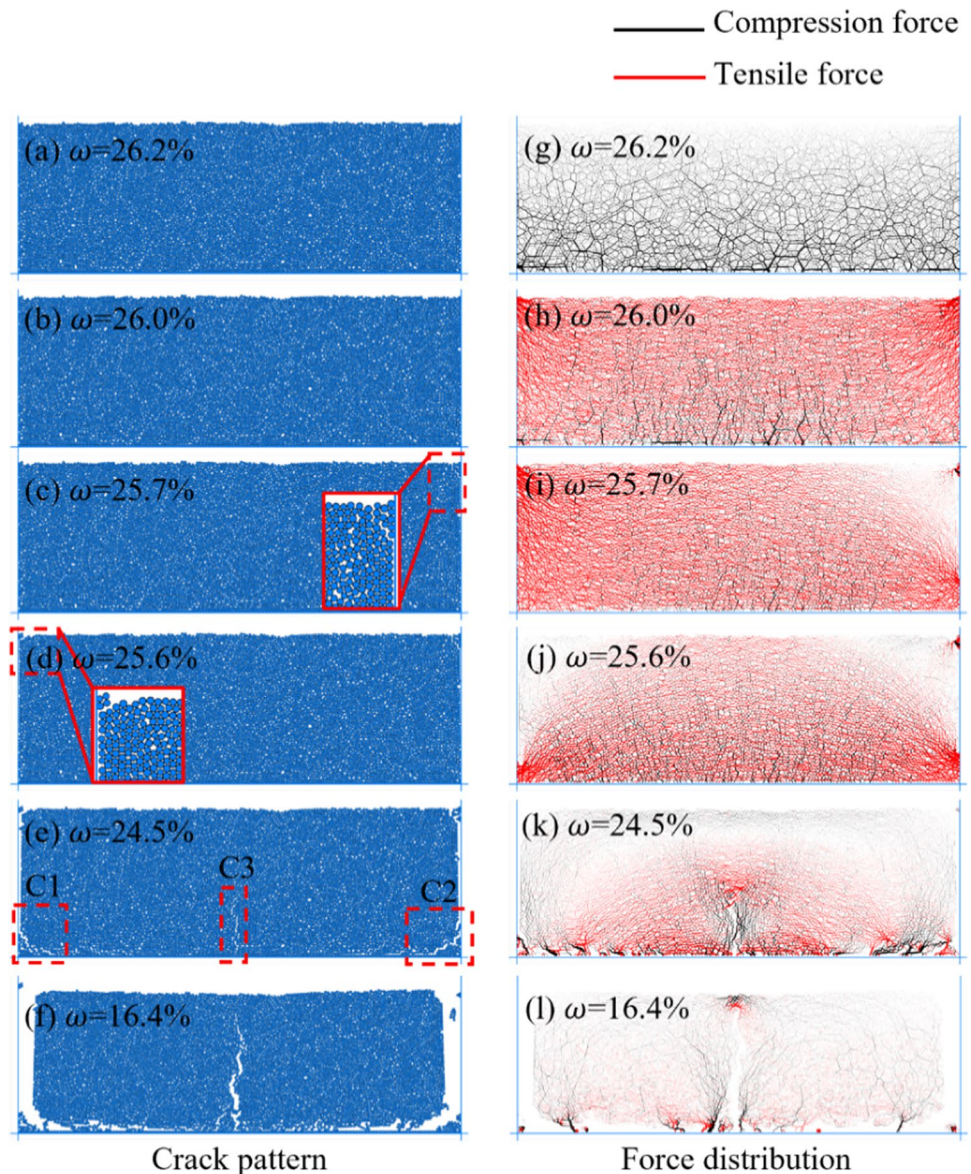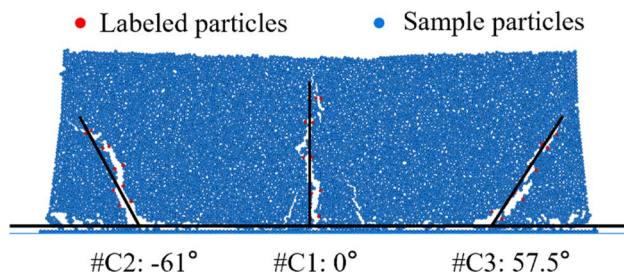
Fig. 11 The angle of the crack and the position of labeled particle in the sample

et al. 2021). Under the constraints of the bottom boundary, the length-to-thickness ratio of the sample may affect the distribution of inter-particle tensile forces.

Shearing effect

As shown in Fig. 11, the cracking angles corresponding to different cracks can be roughly obtained by connecting the particles at the top and bottom of the cracks, respectively. The cracks inclined to the right are defined to have positive angles, while those inclined to the left are negative. Specifically, the angles for Cracks 1, 2, and 3 are measured to be 0°, − 61°, and 57.5°, respectively. For each crack, 5 pairs of particles, distributed on both sides of the crack, are selected as labeled points for data analysis, as shown in Fig. 11.

Table 3 shows the final displacement of the particles on the left and right sides of the three main desiccation cracks. In the table, L and R are used to represent the labeled points on the left and right sides of the crack, respectively. The crack propagation direction is quantified by the crack angle. First, the changes in the coordinates of the corresponding particles in the global coordinates were obtained from the particles. Then, the displacement of the particle along the crack development direction can be calculated through the coordinate axis transformation. Due to the overall shrinkage of the soil, all obtained displacements are all negative values. The displacement of the particles on the right side of the Crack 2 surpasses that on the left. The displacement of the particles on the left side of the Crack 3 is larger than that on the right side. For both cracks 2 and 3, the displacement of the particles inside the crack dip along the crack development direction is smaller than that of the particles outside the crack dip. This difference in displacement along the direction of the failure surface indicates that the desiccation cracks are not only affected by tensile stress during the propagation process, but also influenced by shear stress (Zeng et al. 2020). There is no obvious pattern of particle displacement on both sides of Crack 1, indicating that the crack developed in the middle of the sample bottom is basically not affected by shearing effect.

Figure 12 shows the distribution of the inter-particle shear forces in the sample during crack development, with the darker colors representing larger shear forces. In the case of cracks C2 and C3, the inter-particle shear forces near

Table 3 Final displacement of particles on both sides of the crack along the crack direction (m)

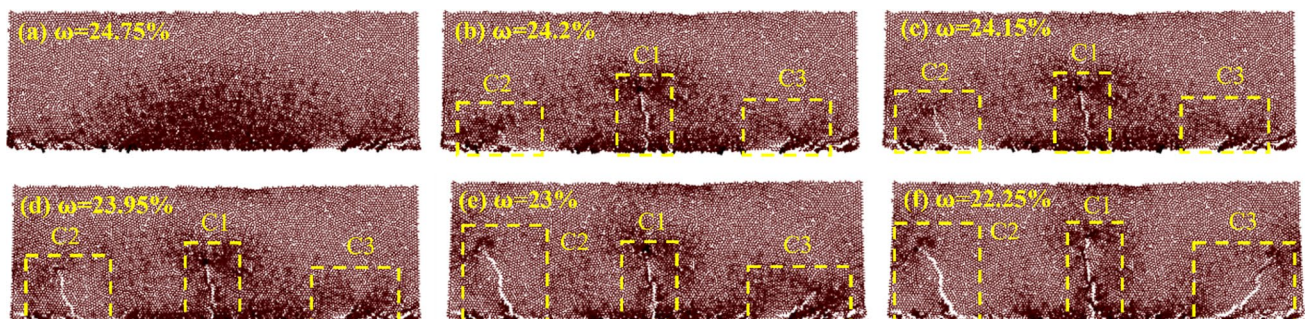| C2(L)	C2(R)	C1(L)	C1(R)	C3(L)	C3(R)
− 2.56E−03	− 2.65E−03	− 1.92E−03	− 1.84E−03	− 1.63E−03	− 1.62E−03
− 2.17E−03	− 2.32E−03	− 1.53E−03	− 1.54E−03	− 1.42E−03	− 1.41E−03
− 1.65E−03	− 1.97E−03	− 1.01E−03	− 1.02E−03	− 1.04E−03	− 1.04E−03
− 1.12E−03	− 1.72E−03	− 4.64E−04	− 4.52E−04	− 6.27E−04	− 5.02E−04
− 7.19E−04	− 1.46E−03	− 9.11E−05	− 5.60E−05	− 2.82E−04	− 1.67E−04

Fig. 12 The distribution of the inter-particle shear forces within the sample during crack development

the side wall regions surpass that at the inner side during propagation, while there is no significant difference around the crack C1. This phenomenon indicates the existence of shearing effect during the development of oblique cracks.

Discussions

The mechanism of radial crack initiation and propagation

In the DEM modeling, the bottom friction constrains the shrinkage of the sample, resulting in the distribution of arched inter-particle tensile force in the sample. It is interesting from the numerical results that the radial cracks at the bottom in this model are basically perpendicular to the inter-particle tensile force, which conforms to the rule of stress-induced cracks (Weinberger 1999). As shown in Fig. 13, the blue line is the inter-particle tensile force distribution field in the sample, while the red dotted line represents the direction of potential crack development. Since the tensile forces are distributed in an arched shape, cracks would theoretically initiate perpendicular to the direction of tensile force. Consequently, cracks in the middle initiate vertically, while those on the sides develop obliquely.

As the micro-cracks originate from the edges and propagate towards the center, the arched tensile force contracts inward. It is also noted that the initiation of cracks will gradually change the inter-particle tensile force distribution. Besides, the shear stress continues to generate new cracks obliquely, because the sample is continuously subjected to frictional force and reverse shrinkage force at the left or right regions of the sample.

Influencing factors of radial cracking

Basal friction

Basal friction has a significant effect on cracking patterns (Groisman and Kaplan 1994; Amarasiri et al. 2011; Zeng et al. 2019). Previous studies show that the bottom-initiated radial cracks were caused by the shearing effect due to basal friction (Zeng et al. 2020). The influence of basal friction includes three aspects: the size of the particles attached to the bottom boundary, the interfacial frictional coefficient, and the interfacial bonding. Holding all other parameters constant, Fig. 14 shows the bottom radial cracks of the sample with different radii of boundary particles. When no particle was attached on the bottom boundary (i.e., particle radius was 0.0 mm), the sample was in direct contact with the flat
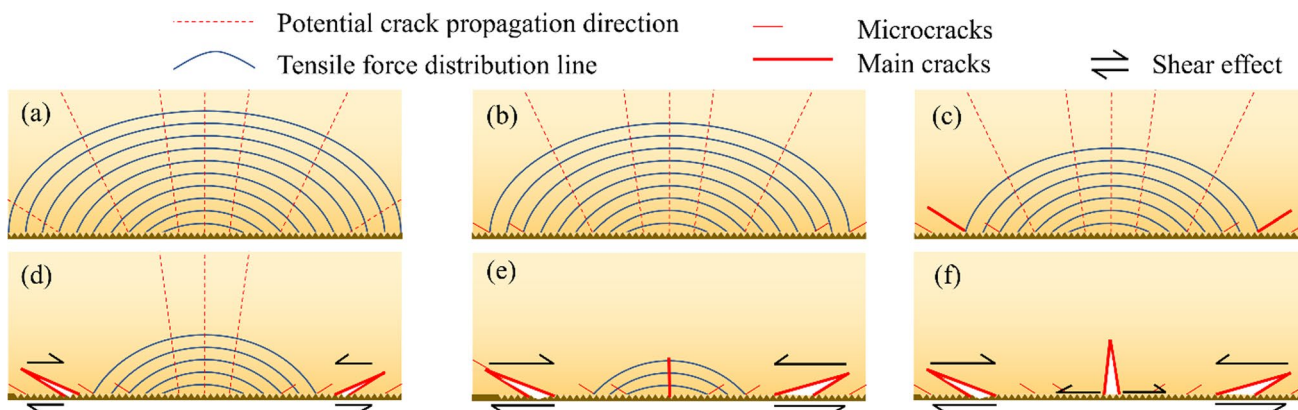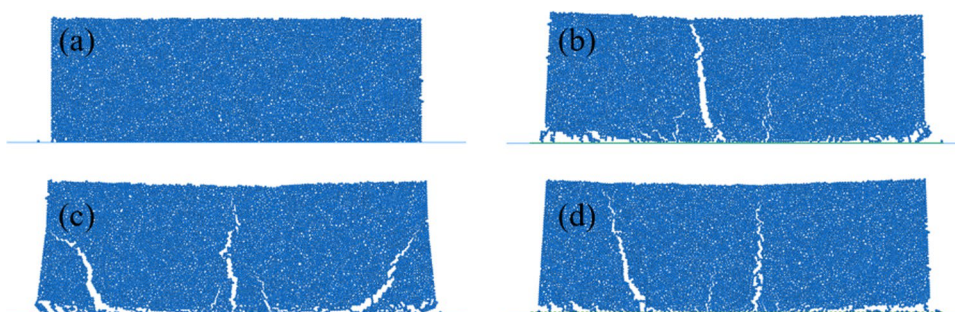

Fig. 13 Schematic view of the radial crack initiation and propagation

Fig. 14 Final cracking pattern in samples with different interfacial roughness where the radii of bottom particles are (**a**) 0.0 mm, (**b**) 0.1 mm, (**c**) 0.3 mm and (**d**) 0.5 mm

surface and no cracks were initiated. As the radius increased to 0.1 mm or 0.3 mm, the number of cracks increased, due to the increased boundary roughness which significantly impacts sample shrinkage. Therefore, the tensile stress in the sample tends to be localized at the bottom, resulting in the initiation of more cracks. However, when the bottom particle radius was 0.5 mm, the number of cracks is less than that with the particle radius of 0.3 mm. It indicates that the number of cracks is not positively correlated with the bottom particle size.

Figure 15 shows the bottom radial cracking patterns when the interfacial friction coefficients were set as 0.05, 0.25 and 0.45, respectively. It was found that the interfacial friction coefficient has no obvious effect on the crack development. The shrinkage of the soil particle may cause detachment of the bottom boundary particles from the sample within a short time. Thus, the model is not sensitive to interfacial friction coefficient in the simulation.

Previous numerical studies have reported a significant impact of the interfacial bonding factor on cracking patterns (Sánchez et al. 2014; Sima et al. 2014; Stirling et al. 2017; Le et al. 2022). Figure 16 shows the final cracking patterns of the samples with different interfacial bond factors d. Similar to the basal particle size effect, the larger the interfacial bonding factor, the more restriction on the sample shrinkage. There was no crack in the sample when the interfacial bonding factor was 0.1. With the increase of interfacial bonding factor, the number of cracks increased, but it was not positively correlated.

Figure 17 shows the evolution of inter-particle force chain distribution of samples with interfacial bonding factor of 0.1 and 10.0. In the modeling, the micro-cracks first initiated in samples of lower interfacial bonding factor. A large number of micro-cracks initiated at the bottom of the sample with an interface bonding factor of 0.1. The internal inter-particle tensile force field was relatively weak at the water content of 25.25%. However, the sample with an interfacial bonding factor of 10.0 only produced a few micro-cracks at the edges, and the interior was mainly distributed with an arched tensile force field. During the subsequent drying, the basal bonds of the sample were broken, and the sample was almost free from boundary resistance during the subsequent shrinkage. As a result, no large cracks occurred. However, the basal bonds in the sample with a larger interfacial bonding factor was not completely broken, and the sample shrinkage continued to be constrained during the drying process. When the local tensile force increased to the tensile strength of the sample, the large cracks initiated and simultaneously weakened the tensile force field.

Evaporation gradient

Due to the small thickness of the simulated soil samples, it was assumed in the model that the water loss in the samples was basically uniform. In practice, during the drying process, an evaporation gradient is present in the soil samples. Herein, the effect of evaporation gradient on the development of basal radial cracks is explored below. As an example, the water loss rate gradient was set to 20% along the vertical direction of the soil layer. It means that the water loss rate of the upper particle layer will be 20% faster than that of the bottom particle layer. Figure 18 shows the final cracking patterns of samples with the evaporation gradient of 0%, 15% and 30%, respectively. The sample in Fig. 18a lost water uniformly. It was found that a higher evaporation gradient would lead to a smaller number of cracks. Compared with the sample of uniform shrinkage, the bottom shrinkage of the sample with gradient water loss was relatively small. The bottom stress caused by the friction constraint is relatively small, making it difficult to initiate more cracks. In other studies, the same conclusion was obtained for thicker samples with explicit consideration of evaporation gradient (Zeng et al. 2019; Lin et al. 2021; Le et al. 2022). The
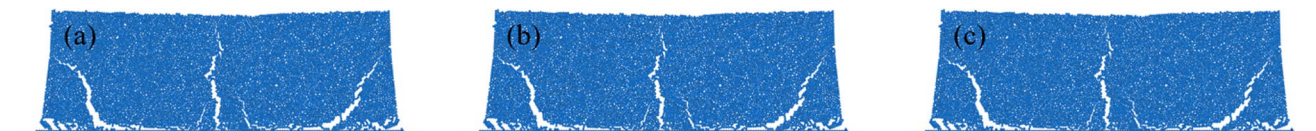

Fig. 15 Cracking pattern in soil samples where the interfacial frictional coefficient was (**a**) 0.05, (**b**) 0.25 and (**c**) 0.45
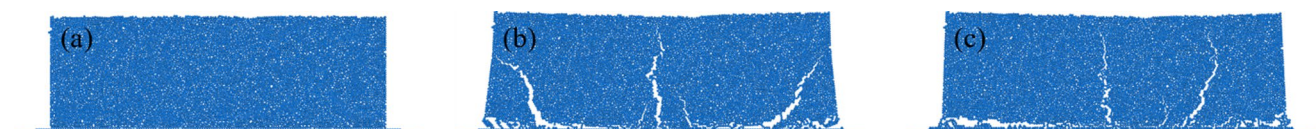

Fig. 16 Cracking patterns in samples where the interfacial bonding factor was (**a**) 0.1, (**b**) 1.0 and (**c**) 10.0

water content at the surface layer is lower during the drying process, so that the tensile strength and effective modulus of the upper part of the sample are always higher than the bottom regions. Due to the relatively higher tensile strength of the upper soil sample, radial cracks were more difficult to propagate upwards.

Shrinkage parameter

The shrinkage parameter is a typical indicator reflecting the material shrinkage potential (El Youssoufi et al. 2005; Péron et al. 2009). A larger shrinkage parameter indicates a higher clay content in the simulated soils (Sima et al. 2014).

Fig. 17 The inter-particle force chain distribution of samples with interfacial bonding factor of 0.1 and 10.0 during the drying process. **a–e** The interfacial bonding factor is 0.1. **f–j** The interfacial bonding factor is 10.0
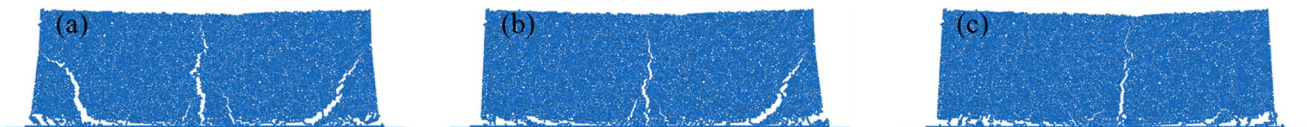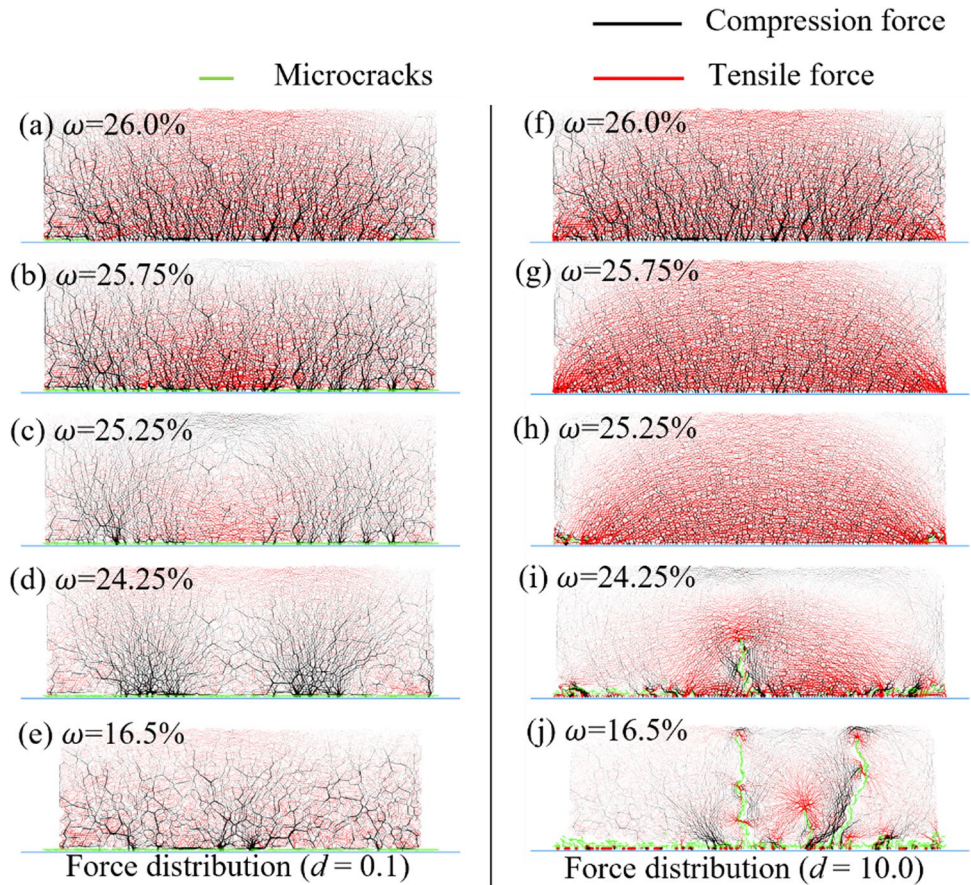
Fig. 18 Crack patterns in samples where the evaporation gradient is (**a**) 0%, (**b**) 15% and (**c**) 30%
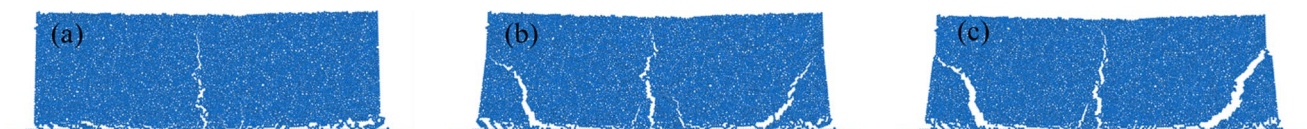
Fig. 19 Cracking patterns in samples with the shrinkage parameter of (**a**) 0.065, (**b**) 0.085 and (**c**) 0.105

Figure 19 shows the effect of the shrinkage parameter on the bottom radial cracks. The final water content of the three samples was constant as 16.4%. The larger the shrinkage parameter, the more cracks and the wider the cracks would be. Under the same bottom boundary constraints, the tensile stress is more concentrated in the samples with large shrinkage parameters. Therefore, it is easy to initiate more cracks. Simultaneously, the larger the shrinkage parameter of the sample, the larger the sample deformation was. In this case, the crack was also wider.

Conclusions

In this study, the discrete-element method (DEM) is employed to simulate the bottom-initiated radial desiccation cracking phenomenon in soil. Through laboratory tests and DEM simulation, the initiation and propagation mechanisms of bottom-initiated radial cracks and its influencing factors were explored. The following conclusions can be drawn:

(1) Laboratory tests revealed a clear correlation between the propagation direction of bottom cracks and their initiation positions. The radial characteristics of the bottom-initiated cracks were observed. The observed soil radial desiccation phenomenon by DEM modeling is in good agreement with experimental observations, which confirms the feasibility of the DEM simulation approach.

(2) The numerical results show that the inter-particle tensile force in the sample was distributed as an arched shape due to the constraint of the bottom boundary. The crack propagation was perpendicular to the inter-particle tensile force. Therefore, the middle cracks developed vertically, while the cracks on both sides of the sample were inclined. The shear stress induced by the combined effect of the basal friction and the reverse shrinkage controlled the cracks on both sides to propagate obliquely.

(3) Several influencing factors of bottom-initiated radial cracks in the simulation were discussed. The rough bottom boundary would enhance the constraint on soil shrinkage, increasing the number of bottom-initiated cracks. The size of the bottom particles and interface bonding factor played a significant role in the effect of basal friction. Compared with the samples under uniform water loss conditions, the bottom shrinkage rate was relatively low for the sample under a gradient water loss. In addition, an increase in the shrinkage parameter of the soil particles led to a greater extent of crack propagation.

The DEM modeling in this study has successfully reproduced the unique radial characteristics of bottom-initiated cracks and improves the understanding of bottom-initiated desiccation cracking phenomenon in soil. This phenomenon is subjected to the control by the special basal boundary conditions and the uniform water loss model. Furthermore, the linear-based contact bond model may not be enough to represent the complex viscoelastic-plastic property and the physical–chemical reaction of the clayey soil. More detailed studies in the future could focus on the mechanical interactions between soil and boundary, the evolution of moisture field and the plastic and ductile properties of the clayey soil to improve the numerical analysis of soil bottom-initiated radial desiccation cracking phenomenon.

Declarations

Competing interests The authors declare no competing interests.

References

Amarasiri AL, Kodikara JK, Costa S (2011) Numerical modelling of desiccation cracking. Int J Numer Anal Meth Geomech 35:82–96. https://doi.org/10.1002/nag.894

ASTM D-2487 (2017) Standard practice for classification of soils for engineering purposes (Unified Soil Classification System). West Conshohocken: American Society for Testing and Materials

Baker R (1981) Tensile strength, tension cracks, and stability of slopes. Soils Found 21:1–17. https://doi.org/10.3208/sandf1972.21.2_1

Chaduvula U, Viswanadham BVS, Kodikara JK (2017) A study on desiccation cracking behavior of polyester fiber-reinforced expansive clay. Appl Clay Sci 142:163–172. https://doi.org/10.1016/j.clay.2017.02.008

Costa S, Kodikara JK, Shannon B (2013) Salient factors controlling desiccation cracking of clay in laboratory experiments. Géotechnique 63:18–29. https://doi.org/10.1680/geot.9.P.105

Costa S, Kodikara J, Thusyanthan I (2008) Modelling of desiccation crack development in clay soils. In: Proc 12th IACMAG Conf 2008:1099–1107

Cui YJ, Gao YB, Ferber V (2010) Simulating the water content and temperature changes in an experimental embankment using meteorological data. Eng Geol 114:456–471. https://doi.org/10.1016/j.enggeo.2010.06.006

Cundall PA, Strack ODL (1979) A discrete numerical model for granular assemblies. Géotechnique 29:47–65. https://doi.org/10.1680/geot.1979.29.1.47

DeCarlo KF, Shokri N (2014) Effects of substrate on cracking patterns and dynamics in desiccating clay layers. Water Resour Res 50:3039–3051. https://doi.org/10.1002/2013WR014466

Duan N, Cheng YP, Xu X (2017) Distinct-element analysis of an off-shore wind turbine monopile under cyclic lateral load. Proc Inst Civil Eng Geotech Eng 170:517–533. https://doi.org/10.1680/jgeen.16.00171

El Youssoufi MS, Delenne JY, Radjai F (2005) Self-stresses and crack formation by particle swelling in cohesive granular media. Phys Rev E 71:051307. https://doi.org/10.1103/PhysRevE.71.051307

Groisman A, Kaplan E (1994) An experimental study of cracking induced by desiccation. Europhys Lett 25:415. https://doi.org/10.1209/0295-5075/25/6/004

Gu M, Cui J, Yuan J, Wu Y, Li Y, Mo H (2022) The stress and deformation of stone column-improved soft clay by discrete element modelling. Eur J Environ Civ Eng 26:1544–1560. https://doi.org/10.1080/19648189.2020.1715851

Guo Y, Han C, Yu X (2018) Laboratory characterization and discrete element modeling of shrinkage and cracking in clay layer. Can Geotech J 55:680–688. https://doi.org/10.1139/cgj-2016-0674

Itasca Consulting Group Inc (2015) PFC^{2D}: particle flow code in 2 dimensions, version 5.0. Minneapolis, MN: Itasca Consulting Group

Jiang NJ, Tang CS, Yin LY, Xie YH, Shi B (2019) Applicability of microbial calcification method for sandy-slope surface erosion control. J Mater Civ Eng 31:04019250. https://doi.org/10.1061/(ASCE)MT.1943-5533.0002897

Kalkan E (2009) Influence of silica fume on the desiccation cracks of compacted clayey soils. Appl Clay Sci 43:296–302. https://doi.org/10.1016/j.clay.2008.09.002

Kodikara JK, Choi X (2006) A simplified analytical model for desiccation cracking of clay layers in laboratory tests. Geotech Spl Publ 147:2558. https://doi.org/10.1061/40802(189)218

Kodikara JK, Nahlawi H, Bouazza A (2004) Modelling of curling in desiccating clay. Can Geotech J 41:560–566. https://doi.org/10.1139/t04-015

Lakshmikantha MR, Reig R, Prat PC, Ledesma A (2013) Origin and mechanism of cracks seen at the bottom of a desiccating soil specimen. In: Proceedings of Geo-Congress 2013: Stability and Performance of Slopes and Embankments III 2013:790–799. https://doi.org/10.1061/9780784412787.0

Le TC, Liu C, Tang CS, Zhang XY, Shi B (2022) Numerical simulation of desiccation cracking in clayey soil using a multifield coupling discrete-element model. J Geotech Geoenviron Eng 148:04021183. https://doi.org/10.1061/(ASCE)GT.1943-5606.0002747

Lin ZY, Wang YS, Tang CS, Cheng Q, Zeng H, Liu C, Shi B (2021) Discrete element modelling of desiccation cracking in thin clay layer under different basal boundary conditions. Comput Geotech 130:103931. https://doi.org/10.1016/j.compgeo.2020.103931

Lin ZY, Tang CS, Yang ZM, Wang YS, Cheng Q, Shi B (2022) Modeling of drying-induced soil curling phenomenon. Water Resour Res 58:e2021WR029749. https://doi.org/10.1029/2021WR029749

Lozada C, Caicedo B, Thorel L (2015) Effects of cracks and desiccation on the bearing capacity of soil deposits. Geotech Lett 5:112–117. https://doi.org/10.1680/geolett.15.00021

Maedo M, Sánchez M, Aljeznawi D, Manzoli O, Guimarães LJ, Cleto PR (2020) Analysis of soil drying incorporating a constitutive model for curling. Acta Geotech 15:2619–2635. https://doi.org/10.1007/s11440-020-00920-0

Miller CJ, Mi H, Yesiller N (1998) Experimental analysis of desiccation crack propagation in clay liners. J Am Water Resour Assoc 34:677–686. https://doi.org/10.1111/j.1752-1688.1998.tb00964.x

Morris PH, Graham J, Williams DJ (1992) Cracking in drying soils. Can Geotech J 29:263–277. https://doi.org/10.1139/t92-030

Nahlawi H, Kodikara JK (2002) Experimental observations on curling of desiccating clay. In International Conference on Unsaturated Soils 2002:553–556. http://arrow.monash.edu.au/vital/access/manager/Repository/monas

Nahlawi H, Kodikara JK (2006) Laboratory experiments on desiccation cracking of thin soil layers. Geotech Geol Eng 24:1641–1664

Péron H, Delenne JY, Laloui L, El Youssoufi MS (2009) Discrete element modelling of drying shrinkage and cracking of soils. Comput Geotech 36:61–69. https://doi.org/10.1016/j.compgeo.2008.04.002

Péron H, Laloui L, Hu LB, Hueckel T (2013) Formation of drying crack patterns in soils: a deterministic approach. Acta Geotech 8:215–221. https://doi.org/10.1007/s11440-012-0184-5

Potyondy DO, Cundall PA (2004) A bonded-particle model for rock. Int J Rock Mech Min Sci 41:1329–1364. https://doi.org/10.1016/j.ijrmms.2004.09.011

Rayhani MHT, Yanful EK, Fakher A (2007) Desiccation-induced cracking and its effect on the hydraulic conductivity of clayey soils from Iran. Can Geotech J 44:276–283. https://doi.org/10.1139/T06-125

Sánchez MJ, Manzoli OL, Guimaraes LJN (2014) Modeling 3-d desiccation soil crack networks using a mesh fragmentation technique. Comput Geotech 62:27–39. https://doi.org/10.1016/j.compgeo.2014.06.009

Shin H, Santamarina JC (2011) Desiccation cracks in saturated fine-grained soils: particle-level phenomena and effective-stress analysis. Géotechnique 61:961–972. https://doi.org/10.1680/geot.8.P.012

Sima J, Jiang M, Zhou C (2014) Numerical simulation of desiccation cracking in a thin clay layer using 3D discrete element modeling. Comput Geotech 56:168–180. https://doi.org/10.1016/j.compgeo.2013.12.003

Stirling RA, Glendinning S, Davie CT (2017) Modelling the deterioration of the near surface caused by drying induced cracking. Appl Clay Sci 146:176–185. https://doi.org/10.1016/j.clay.2017.06.003

Tang CS, Cui YJ, Tang AM, Shi B (2010) Experiment evidence on the temperature dependence of desiccation cracking behavior of clayey soils. Eng Geol 114:261–266. https://doi.org/10.1016/j.enggeo.2010.05.003

Tang CS, Shi B, Liu C, Suo WB, Gao L (2011) Experimental characterization of shrinkage and desiccation cracking in thin clay layer. Appl Clay Sci 52:69–77. https://doi.org/10.1016/j.clay.2011.01.032

Tang CS, Pei XJ, Wang DY, Shi B, Li J (2015) Tensile strength of compacted clayey soil. J Geotech Geoenviron Eng 141:04014122. https://doi.org/10.1061/(ASCE)GT.1943-5606.0001267

Tang CS, Zhu C, Cheng Q, Zeng H, Xu JJ, Tian BG, Shi B (2021) Desiccation cracking of soils: a review of investigation approaches, underlying mechanisms, and influencing factors. Earth Sci Rev 216:103586. https://doi.org/10.1016/j.earscirev.2021.103586

Tran KM, Bui HH, Sánchez M, Kodikara J (2020) A DEM approach to study desiccation processes in slurry soils. Comput Geotech 120:103448. https://doi.org/10.1016/j.compgeo.2020.103448

Tran KM, Bui HH, Nguyen GD (2021) Hybrid discrete-continuum approach to model hydromechanical behaviour of soil during desiccation. J Geotech Geoenviron Eng 147:04021102. https://doi.org/10.1061/(ASCE)GT.1943-5606.0002633

Vo TD, Pouya A, Hemmati S, Tang AM (2017) Numerical modelling of desiccation cracking of clayey soil using a cohesive fracture method. Comput Geotech 85:15–27. https://doi.org/10.1016/j.compgeo.2016.12.010

Weinberger R (1999) Initiation and growth of cracks during desiccation of stratified muddy sediments. J Struct Geol 21:379–386. https://doi.org/10.1016/S0191-8141(99)00029-2

Xu JJ, Tang CS, Cheng Q, Vahedifard F, Liu B, Shi B (2022) Monitoring and early detection of soil desiccation cracking using distributed fiber optical sensing. Géotechnique 1–43. https://doi.org/10.1680/jgeot.21.00397

Zeng H, Tang CS, Cheng Q, Inyang HI, Rong DZ, Lin L, Shi B (2019) Coupling effects of interfacial friction and layer thickness on soil desiccation cracking behavior. Eng Geol 260:105220. https://doi.org/10.1016/j.enggeo.2019.105220

Zeng H, Tang CS, Cheng Q, Zhu C, Yin LY, Shi B (2020) Drought-induced soil desiccation cracking behavior with consideration of basal friction and layer thickness. Water Resour Res 56:e2019WR026948. https://doi.org/10.1029/2019WR026948